

***Final Draft***  
of the original manuscript:

Huetsch, L.L.; Hilgert, J.; Herzberg, K.; dos Santos, J.; Huber, N.:  
**Temperature and Texture Development during High Speed  
Friction Stir Processing of Magnesium AZ31**  
In: Advanced Engineering Materials (2012) Wiley

DOI: 10.1002/adem.201200112

DOI: 10.1002/2012XXXX

## Temperature and Texture Development during High Speed Friction Stir Processing of Magnesium AZ31\*\*

By Leon Leander Hütsch\*, Jakob Hilgert, Klaas Herzberg, Dr. Jorge dosSantos, Prof. Dr. Norbert Huber

[\*] Helmholtz-Zentrum Geesthacht, Institute of Materials Research, Materials Mechanics, Solid-State Joining Processes - WMP, Geesthacht, Germany - Tel:+49 4152 872067 - Fax:+49 4152 872033

[\*\*] The author gratefully acknowledges the Helmholtz-Zentrum Geesthacht (HZG) for funding this research.

---

### Abstract

The increasing demand for low weight structural materials yields a growing interest in Mg alloys. To make the use of these materials interesting for industrial applications, high processing speeds and process reliability is essential. Therefore one aim of this work is to develop defect free high speed friction stir welds in the range of 1 m/min to 10 m/min using rolled Mg AZ31 as base material. All processing parameters are selected to generate a minimum in grain size. The resulting welds are subjected to temperature field and texture development investigations. Using finite element methods, the energy input per unit length as well as the temperature development around the tool at high processing speeds is predicted. Within the chosen parameter range, image correlation is used to evaluate distortion of the processed samples. Thermocouples are used to measure the temperature during processing and to calibrate subsequently the numerical calculations. Grain size and morphology as well as the texture evolution are investigated using EBSD analysis. This study shows that while ensuring a constant weld quality the energy input per unit length and sample distortion can continuously be decreased while increasing processing speed. Thermal analysis extended by numerical investigations reveal a strong thermal field asymmetry between AS and RS with maximum temperatures ranging between 470°C

and 300°C. EBSD investigated reveal a continuously decreasing grain size with increasing processing speed reaching a threshold at processing speeds of 5 m/min. The basal planes exhibits a gradual shift from 0° within the base material to 45° into processing direction for the processed samples with increasing processing speed.

Keywords: Friction Stir Processing, Friction Stir Welding, Magnesium, AZ31, High Speed

## 1. Introduction

As summarized by Eliezer et al. the development of more economical and ecological products will be one of the most urgent challenges an increasingly industrialized world has to face.<sup>[1]</sup> To meet these demands, one promising approach is the reduction of weight by using lightweight structures. Even though Al is nowadays the material of choice when it comes to weight reduction, Mg offers an even greater weight saving potential. Aghion et al. describe magnesium alloys to be up to 35% lighter than aluminum and to have an excellent strength to weight ratio.<sup>[2]</sup> Bichler et al. explain the challenges and opportunities during casting of Mg alloys and Fechner et al. investigated the recycle ability.<sup>[3,4]</sup> The challenges and potentials of Mg alloys in the automotive industry is elucidated by Friedrich et al. as well as Kulekci et al.<sup>[5,6]</sup> Their applicability however is limited by the inherent poor formability, mostly arising from the hexagonal crystal structure explained by Kleiner et al.<sup>[7]</sup> In two extensive publications, Barnett et al. describe the limits of formability and the development of twinning partly due to the lack of sufficient slip systems at room temperature.<sup>[8,9]</sup> An increase in working temperature would pose a solution, but due to time, cost and feasibility this is often not an option for industrial applications. Another approach to increase formability could be grain refinement as described by Matsubara et al.<sup>[10]</sup> Investigations conducted by Watanabe et al. show that small grains enable grain

boundary sliding and grain rotation leading to improved ductility.<sup>[11]</sup> Grain refinement of the necessary magnitude can be achieved by Friction Stir Processing (FSP) as shown by Charit et al.<sup>[12]</sup> FSP was invented by Mishra et al. and is based on Friction Stir Welding (FSW), which was conceived by Thomas et al. at TWI, LTD., UK.<sup>[13,14]</sup> As shown by Mishra et al. and Esparza et al. FSP has proven to be a suitable tool for grain refinement over a wide range of applications and materials including Magnesium.<sup>[15,16]</sup> Using FSP on AZ31 Chang et al. were able to obtain grain sizes in the range of 80 - 130 nm.<sup>[17]</sup>

Another way of altering the mechanical properties of a given material is by changing its texture. Gehrman et al. showed, that for Mg with its limited amount of available slip systems, tailoring the texture has a particularly large effect.<sup>[18]</sup> As shown by Mukai et al., orientating the available slip systems into the preferred direction of deformation yields an improved formability behavior.<sup>[19]</sup> FSP, incorporating the ability to locally tailor grain size and texture, could therefore be introduced as an intermediate step in a process chain if extensive deformation due to forming is necessary. The hereby introduced local microstructural changes can be precisely positioned at locations in which high amounts of deformation are required. Considering weight reduction in the automotive area, Mg crash elements produced and modified by FSW / FSP could be tailored to securely fail at defined positions. Especially in the automotive area but also in other industries, the process speed is of a critical importance.

To the author's best knowledge, the highest feed rate (h. a. processing speed) in FSW/FSP of AZ31 published in literature was achieved by Cao et al. reaching 1.8 m/min, clearly falling behind traditional laser welding which can easily reach 5 m/min.<sup>[20,21]</sup> Therefore, one scope of this work was to obtain suitable processing

parameters for defect free process zones using processing speeds in the range of 1 - 10 m/min.

## 2. Experimental

### Material and Setup

High Speed Friction Stir Processing (HS-FSP) was performed on commercially available Mg AZ31 sheet material with the following composition: 2.9wt.% Al, 0.74wt.% Zn, 0.29wt.% Mn, and small portions of Si, Ni and Cu. HS-FSP was carried out as a single pass over the entire sheet length in a bead on plate configuration incorporating a "Run-In - Run-Off" approach. With this approach, a sheet of the identical material is clamped in front and behind the sheet which is to be investigated. This way the acceleration path of the machine as well as the end hole are displaced onto a dummy sheet as seen in Fig.1. In order to obtain comparable clamping setups, all screws fixing the plate to the table and backing bar have been tightened to 25 Nm.

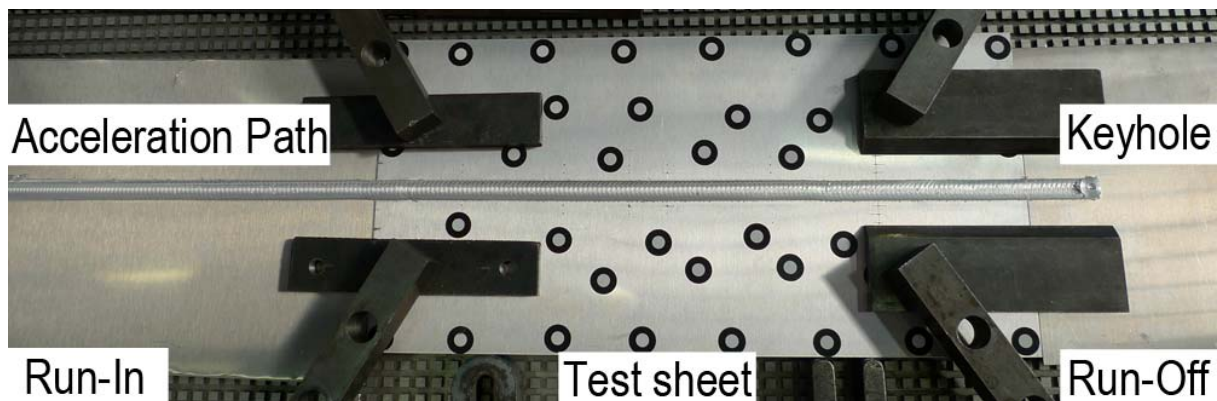


Figure 1: Setup of the sample together with the Run In and Run Off sheets. The acceleration of the machine to the desired processing parameters was done on the Run In sheet before transitioning onto the actual sample. The keyhole which is presented at the end of the bead is positioned on the Run Off Sheet.

## Machine and Tool

FSP was performed in force control mode on a Tricept T805 five axis parallel kinematic robot incorporating an independent force control unit acting as a sixth axis. In this study, a modular tool with adjustable pin length was utilized. A tapered threaded pin with three flats having a diameter from 5 to 3 mm was set to a length of 1,8 mm and a was applied in conjunction with a 17 mm diameter double scrolled shoulder. Pin and shoulder were made out of Hotvar 55 Cr Mo V 10 23 9 hot working steel.

## Parameter Development

Investigations have been conducted in rolling direction (RD), transverse to rolling direction (TD) and in 45° to the rolling direction (45°). The sheet dimensions were 2 \* 490 \* 200 mm for RD -, 2 \* 390 \* 200 mm for TD -, and 2 \* 350 \* 200 mm for 45° specimens. The process parameters were developed with the aim of creating defect free welds using as little heat input as possible. As the processing speeds ( $V_p$ ) were preset to 1,3,5,7 and 10 m/min, the remaining parameters affecting the heat input were rotational speed (RPM) or vertical force ( $F_z$ ) which were systematically increased until the process area had an acceptable surface finish e.g. limited flash and no obvious surface discontinuities. In order to rule out lack of penetration defects, the samples were subsequently cut transverse to processing direction and polished to be investigated by optical microscopy. The final processing parameters are given in Tab.1.

Table 1: Machine parameters used in this study.

Processing Speed (Vp) [m/min]	Axial Force (Fz) [kN]	RPM [1/min]	RPM / Vp [rot / mm]
1	8	2000	2.00
3	14	2250	0.75
5	15	2500	0.50
7	15	3250	0.46
10	20	3500	0.35

### Distortion Analysis

Distortion measurements were undertaken using a commercial digital image correlation (DIC) system. In order to measure the distortion, markers were applied to the surface of the plates, leaving the path of the tool free for processing as shown in Fig.2. Images were taken before and after processing. The deformation can be calculated hereafter from the differences between the two states. More details on the working principle of the DIC-System used can be found on the homepage of the GOM GmbH.<sup>[22]</sup>

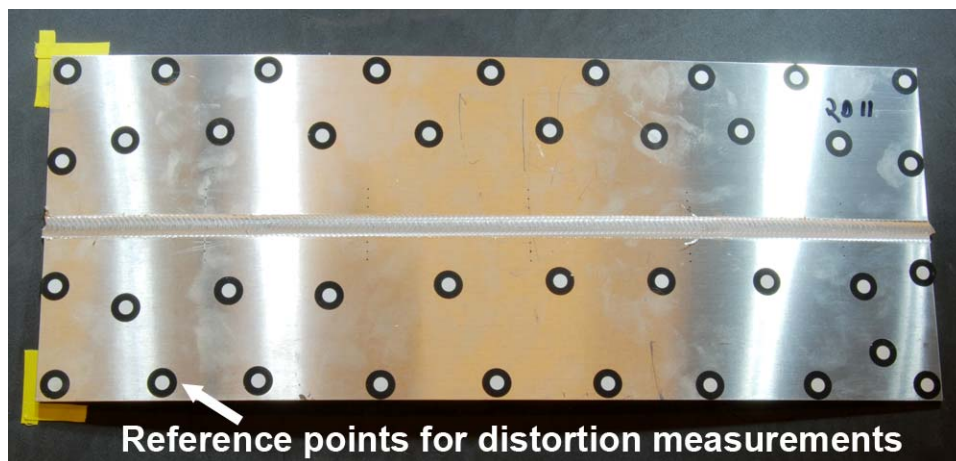


Figure 2: Plate after processing with markers for distortion measurement.

## Temperature Measurements

In order to calibrate the applied thermal model temperature measurements were conducted during processing using type-k thermocouples with 0.5 mm diameter. The thermocouple measuring range was from  $-270^{\circ}\text{C}$  to  $+1372^{\circ}\text{C}$ . The data acquisition system had a maximum sampling rate of 70 Hz. Holes with a diameter of 0,6 mm were drilled into the sheet at positions 10, 15 and 20 mm away from the weld center line as shown in Fig.3. To improve the conductivity and ensure a homogeneous temperature distribution between thermocouple and plate, the drilled holes were filled with conductive silver paste before the thermocouples were inserted.

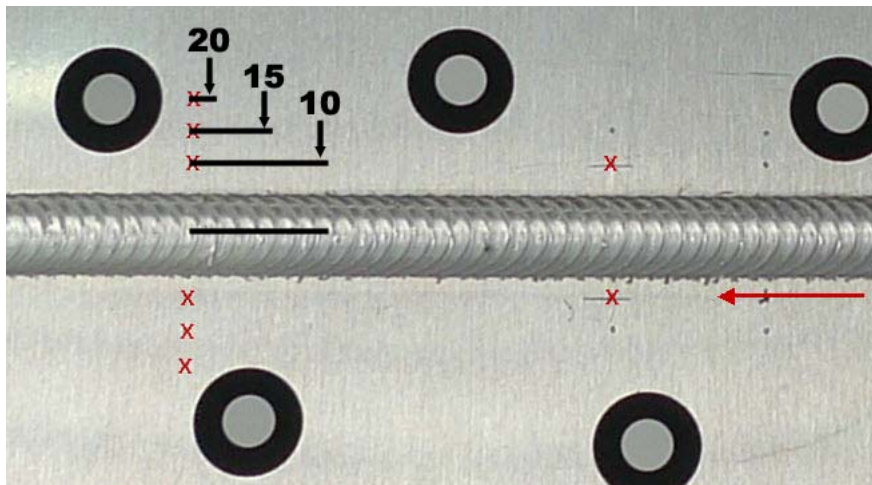


Figure 3: Position of the thermocouples at two different locations along the processing line in distances of 10, 15 and 20 mm from the weld center.

As the programmed and actual weld paths differ from each other due to elasticity in the handling system, the exact position of the thermocouples to the weld center have been measured after processing. This has been done by grinding; polishing and etching the segment of the weld in which the thermocouples have been positioned and subsequently measuring the distance to the weld center using an optical

microscope. The obtained thermal information was subsequently used to calibrate the numerical thermal field analysis for a precise prediction of the temperature field under the tool.

### Microstructural and Texture Analysis

EBSD analysis has been conducted to investigate the texture evolution during processing. Herein the SZ has been investigated in processing direction (PD) using cross sections of the samples. Prior to investigation, the samples have been ground and polished but not etched. A JOEL JSM-6490LV was used with an acceleration voltage of 25 kV, 15 mm of working distance and a spot size of 66. Orientation mapping using automatic beam scanning was carried out with a step size of 0.5 - 2  $\mu\text{m}$ . The average confident index (CI) for all investigated samples was within the order of  $\text{CI} \approx 0.3$  as comparison measurements performed by TSL on fcc material showed a 95% probability of correctly indexed pattern if the CI is above 0.1.<sup>[23]</sup> Grains comprising more than three pixels were removed from the scanned maps using the inherent grain dilatation method in the TSL software ensuring the up most reliability of the obtained microstructural picture. Perturbing boundaries which are often caused by orientation noise were removed by a  $2^\circ$  lower limit boundary disorientation cut off. Low angle boundaries (LAB) were separated from high angle boundaries (HAB) by using the  $15^\circ$  criterion. Grain size measurements have been done using the analysis software inherent line intercept method.

### 3. Thermal Field Modeling

Besides the process induced plastic deformation, the resulting temperature distribution during processing plays a major role in the microstructural evolution of the processed material. In order to gain further insight into the recovery and recrystallization processes during and after FSP, thermal field analysis has been undertaken. The model chosen is based on previous work conducted by Hilgert et al. in which he validated his predictions for bobbin tool FSW.<sup>[24]</sup> To ensure the predicted values to mirror the actual thermal state the model has been calibrated using thermocouple measurement data obtained during processing. The calibration has been conducted in several steps. First, the distance between the drilled thermocouple holes and the tool shoulder has been measured in cross sections cut from the processed samples. Next the thermal data at the given points were programmatically aligning to the predicted thermal data. Finally the thermal model was adapted to the newly acquired reference points. The model itself was implemented in Comsol Multiphysics<sup>TM</sup> and represents the 3D geometry of the experiment featuring backing, plate and tool as shown in Fig.4.

The model is meshed with  $\approx 110000$  quadratic tetrahedral elements as seen in Fig.5. The mesh density is highest in the vicinity of the tool to plate interface where heat is generated. The different processing speeds are implanted by changing the material feed velocity from the input to the output side of the plate domain. A thermal-pseudo-mechanical (TPM) heat source as introduced by Schmidt et al. was used to predict the energy input based on the temperature dependent flow stress  $\tau(T)$  of the material.<sup>[25]</sup> This data is derived from yield stress data compiled by Avedesian et al. according to Eq: 1.<sup>[26]</sup>

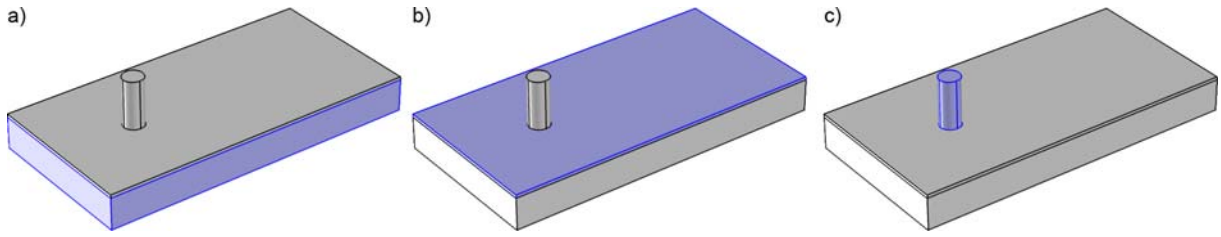


Figure 4: Modelled Domains: Backing a), Plate b) and Tool c).

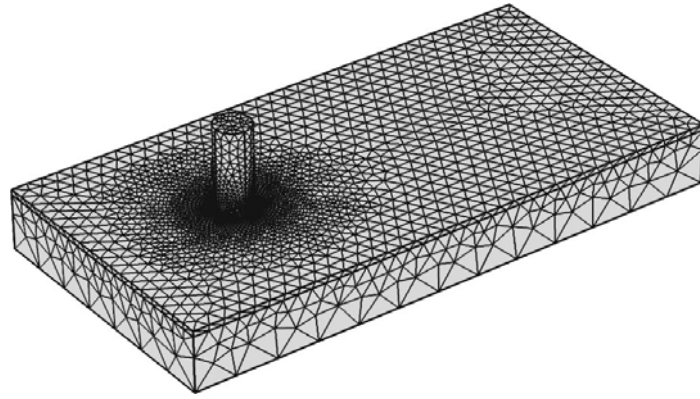


Figure 5: Mesh of the Thermal Model.

$$\tau = \frac{\sigma_y \cdot (T[^\circ\text{C}] + 273.3)}{\sqrt{3}} \quad (1)$$

The heat generation at the interface between the tool surface and the plate material is determined according to the TPM equation:

$$q = \omega \cdot \tau(T) \cdot r \quad (2)$$

$q$  is hereby the surface energy source,  $\omega = 2 \cdot \pi \cdot r$  is the angular velocity of the tool and  $r$  is the distance of a surface element to the axis of rotation. The governing equation of the FE model is the heat transfer equation

$$\nabla(-k\nabla T) = Q - \rho c_p u \nabla T \quad (3)$$

The boundary conditions include convective cooling to the tool, the backing and the

surrounding air according to

$$-n(-k\nabla T + \rho c_p u T) = q + h(T_{inf} - T) \quad (4)$$

where  $n$  is the surface normal vector,  $k$  is the thermal conductivity,  $T$  is the temperature,  $\rho$  is the density,  $c_p$  is the specific heat capacity,  $u$  is the convection term in heat transfer equation,  $h$  is heat transfer coefficient to the tool, backing or air respectively in which  $h$  is the same for the tool and backing,  $q$  is the prescribed inward surface heat flux and  $T_{inf}$  is the external temperature.

The convective energy transport term  $u$  in Eq: 3 is constructed as a superposition of welding speed which is implemented in the plate, the rotation of the tool which is implemented in the tool, and the analytical shear layer velocity with the region of the shear layer in the plate and under the tool.  $u$  is hereby constructed of the tangential velocity  $u_x = V_p - y/r \cdot v_{tan}(r)$  and  $u_y = x/r \cdot v_{tan}(r)$  in the plate / shear layer region. Within the tool,  $u$  is constructed of  $u_x = -\omega x$  and  $u_y = \omega y$ .

As the hot material is extruded around the tool moving through the plate, energy is transported not only by conduction but also by convection. In order to model the asymmetric temperature field characteristic for FSP, this effect must be considered. Therefore an analytical shear layer expression is used to prescribe convective energy transport around the tool according to Eq. 5

$$\begin{aligned} dz &= t_p / 2 - z \\ r_0 &= -dz \cdot \tan(\alpha_p) \\ dr &= r - r_0 \\ \zeta &= dz / t_p \\ \dot{r} &= (1 - \zeta^{m_{shape}}) \cdot (r_s - r_0) + r_0 \\ r_{fade} &= \max((r - r_{star}), 0) \\ \rho &= \max(dr / r_{star}, 0) \\ v_{tan} &= \max(\omega \cdot r \cdot (1 - (\zeta^{m_z} \cdot \rho^{m_r}) - (r_{fade} / r_{sl})^{m_{fade}}), 0) \end{aligned} \quad (5)$$

in which  $t_p$  is the plate thickness,  $r$  is the distance to the rotational axis,  $\alpha_p$  is the cone angle of the pin and  $r_{fade}$ ,  $m_{shape}$ ,  $r_{star}$ ,  $m_z$ ,  $m_r$  and  $r_{sl}$  are shape parameters calibrated from micrographs.

An example for the resulting shear layer velocity profile is given in Fig.6 a). The resulting asymmetry of the temperature field is shown in Fig.6 b).

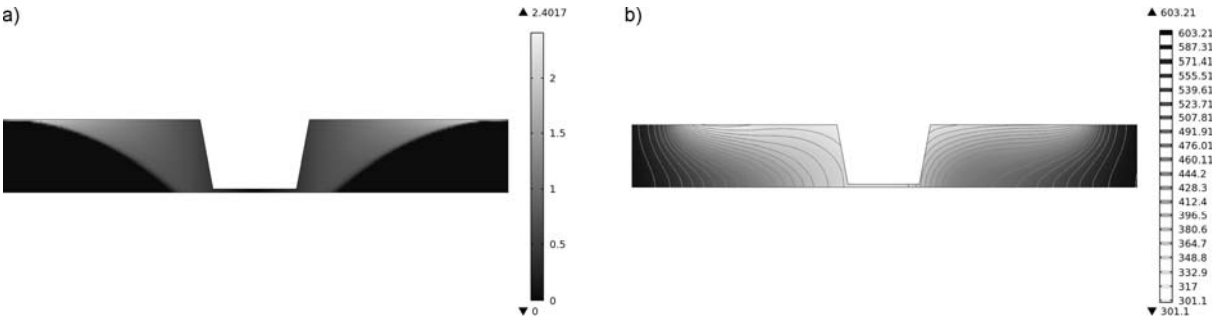


Figure 6: Exemplary results of the numerical thermal Predictions. Shear Layer Velocity [m/s] field around the pin a). Asymmetric thermal field [K] around the Pin b).

The model can also be used to predict the Energy Input per Unit Length (EIUL) by integrating the total heat generation over the interface area between the tool and the plate.

#### 4. Results and Discussion

##### 4.1. Energy Input

Using the model described in Sec. 3 the EIUL could be calculated. The results are plotted over  $V_p$  and can be seen in Fig.7. The overall shape of the curve can be described as continuously decreasing. In detail it can be seen, that the reduction in energy input is divided into two sections. Herein the turning point appears to be at a

processing speed of 5 m/min or at a RPM / Vp ratio of 0.5 rot/mm respectively. It can be noticed that in section I of Fig.7 the decrease in EIUL is much steeper than in section II. In order to investigate this regression more thoroughly, additional processing trials were conducted at 0.8 and 2 m/min. The machine parameters for these trials were found to be Fz=7 kN, RPM= 1750 rpm and Fz=10 kN, RPM=2150 rpm respectively. As these trials were used solely to further comprehend the prementioned decrease, no additional investigations were conducted upon them.

The observed decrease is directly correlated to the processing parameters as rotational speed and axial force are not proportionally raised with increasing Vp. Besides this correlation to the preselected processing parameters, the decrease in EIUL also depicts a physical phenomenon, resulting in the presumption that FSP/FSW can be performed at significantly lower heat inputs than what is currently discussed in the literature. It should be noted, that higher values in EIUL e.g. by increasing rpm or axial force will still create defect free welds but are not investigated in this study since the aim was to introducing as little heat as possible to keep the resulting grain size at a minimum. This becomes further noticeable when considering the ratio between rotational - and processing speeds RPM/Vp as shown in Tab.1. At Vp of 10 m/min, the RPM/Vp ratio decreases to 0,35 rot / mm resulting in  $\approx 3$  mm of travel before the center of the pin performs one full rotation. At the outer circumference of the pin, using a diameter of  $\approx 4$  mm, the material will have to travel  $\approx 12,6$  mm around the pin while being translated 3 mm into processing direction. The additional translational movement leads to the conclusion, that the governing deformation processes in High Speed FSP should be subdivided into a stirring and an extrusion component. This distinction is especially important in regard to the recrystallization behavior and texture development as the level of dynamic recovery in Mg due to extrusion is sufficiently low to allow dynamic recrystallization above a

temperature of 240°C. Thus, after deformation, fine grains can be formed at initial grain boundaries, strengthening the material due to the substructures from dynamic recrystallization. AZ31 in particular work-hardens in the range between 180 - 240°C by deformation mechanisms induced by twinning as described by Friedrich et al.<sup>[27]</sup> It can therefore be argued that the two deformation processes, stirring and extrusion, are contributing to the formation of the process zone in which the thermal input is mainly attributed to stirring whereas plastic deformation to stirring as well as extrusion.

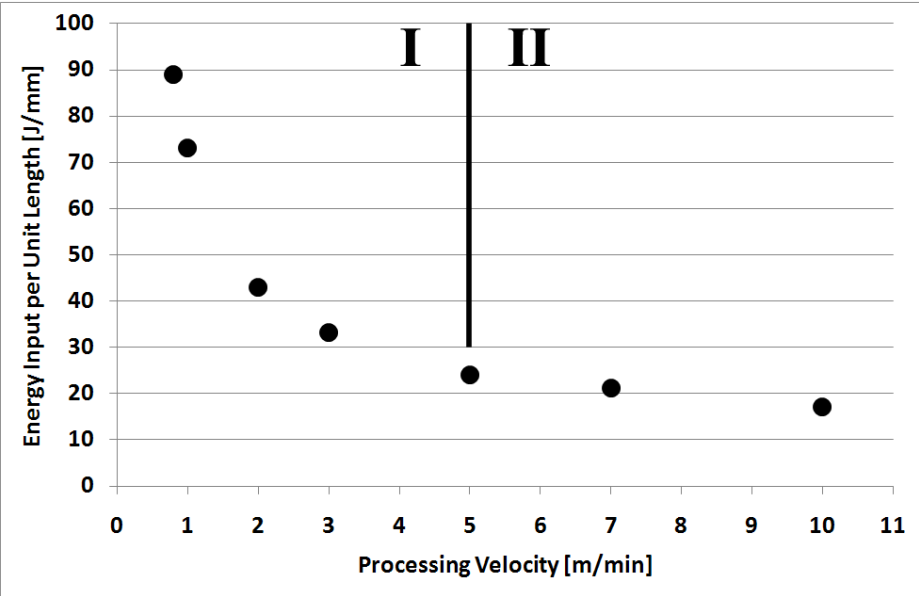


Figure 7: The energy input per unit length as a function of processing velocity. The curve can be divided into two sections, corresponding to high and low decrease in EIUL over the processing velocity field of 5 m/min.

#### 4.2. Distortion

In order to compare samples processed at different velocities to one another, the maximum in distortion has been evaluated by fitting a fifth degree polynomial onto the data points, creating a fit surface as shown in Fig.8 a). Subsequently this shape was

examined by a search algorithm to find the global maximum which was then used as the maximum distortion value and plotted over  $V_p$  as seen in Fig.8 b). From this it can be derived, that maximum distortion decreases with increasing  $V_p$ . Hereby the greatest differences can be found between 1 and 5 m/min exhibiting a drop in maximum deformation of  $\approx 2$  mm. Between 5 to 10 m/min on the other hand the maximum distortion values lie all within a small window of  $\approx 0,5$  mm.

These effects can be directly correlated to the decrease in EIUL which becomes evident when comparing Fig.7 to Fig.8 b). As  $V_p$  is increased the thermal input is minimized, reducing the distortion. Thus, distortion can be minimized by decreasing the EIUL which, in conjunction with high  $V_p$  would satisfy industrial needs. Additionally to the energy input analysis the influence of  $V_p$  and temperature on distortion has been investigated using a 3D DIC-System. The sheet distortion has been calculated by assessing the difference between the undeformed and the deformed state of the sheet. In

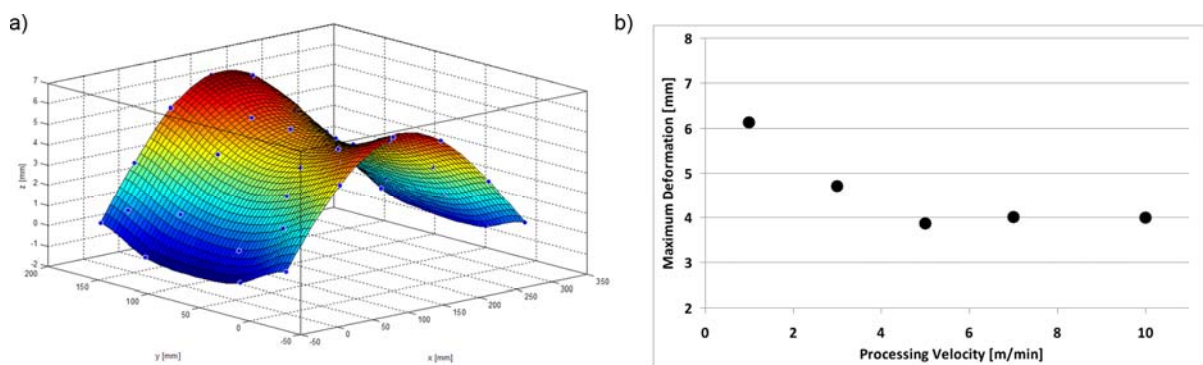


Figure 8: Polynomial fit through the difference in distortion gathered before and after processing and indicated by the reference points a). Values of maximum distortion for all tested processing speeds b).

### 4.3. Temperature

The temperature fields around and directly under the tool during processing were

predicted by a thermal model which was calibrated by thermocouple measurements (section 3). This gave the possibility to characterize the temperature distribution of different  $V_p$  and compare them to each other as presented in Fig.9 a).

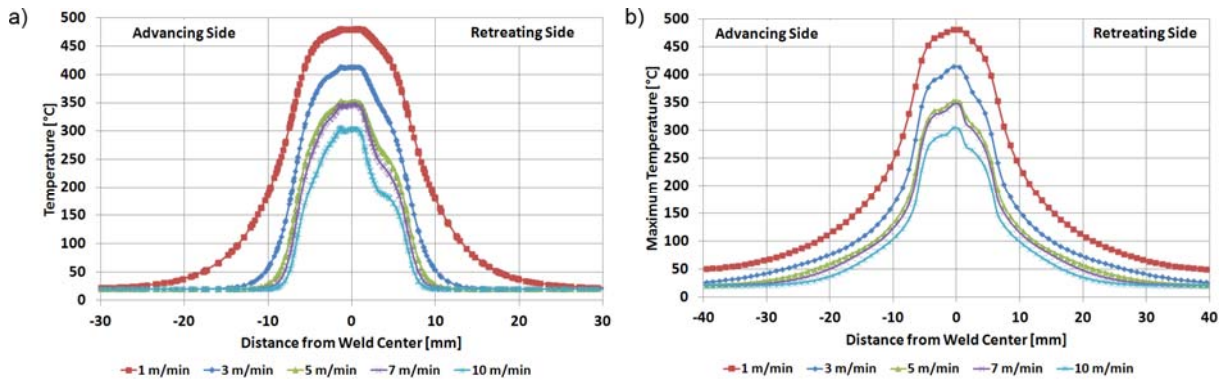


Figure 9: The thermal field was constructed by using a TPM model with the thermal data obtained by the thermo couples as input parameters. Momentary temperature field directly at the tool for different processing speeds a). Maximum temperature field for different processing speeds b).

Fig.9 shows two plots in order to differentiate between the momentary and maximum temperatures occurring during processing which arise from the retardation in thermal conductivity leaving the maximum temperatures, at a given point from the weld center, trailing behind the tool. This discrimination is important as dynamic recrystallization in the circumference of the tool occurs within the momentary temperature regime whereas recovery processes occurring after the tool has passed are aided by the maximum available temperature. The model predicts that during processing the overall maximum temperatures are located around the pin. With increasing  $V_p$  the maximum temperature decreases from  $\approx 470^\circ\text{C}$  for  $V_p$  of 1 m/min to  $\approx 300^\circ\text{C}$  for  $V_p$  of 10 m/min as the RPM/ $V_p$  ratio decreases. The overall maximum temperature is valid for the momentary as well as the maximum temperature state, the former is visible in Fig.9 a) and 9 b). Even though in both plots of Fig.9 a strong

asymmetry between the advancing (AS) and retreating side (RS) can be made out the causes are different. For the momentary temperature (Fig.9 a)) the RS exhibits a steeper decrease in temperature gradient than the AS. This effect becomes more pronounced for faster  $V_p$  and can mainly be attributed to the higher amount of frictional heat at the AS as the RPM/ $V_p$  ratio decreases. Considering the maximum temperatures (Fig.9 b)) the AS still exhibits higher temperatures, even though in contrast to the results in Fig.9 a) the asymmetry between AS and RS decreases with increasing  $V_p$  clearly depicting a difference in material flow as a function of processing speed. Within the  $V_p$  range of 1 to 5 m/min, the resulting maximum temperatures are strongly affected by the material transport around the tool. As the material is picked up at the AS, heated up by friction, transported around the pin and deposited again at the advancing side, higher temperatures are reached.

Above  $V_p$  of 5 m/min, the importance of material transport around the tool lessens as extrusion phenomena come into play yielding a strong asymmetric temperature distribution. This division into two distinct maximum temperature regimes fits well to the calculated decrease in energy input as previously described in section 4.1. Additionally to the effect of asymmetry, a distinct difference in the temperature convergence within the different  $V_p$  with increasing distance from the weld center can be noticed. For the momentary temperature (Fig.9 a)) the curves between  $V_p$  of 3 - 10 m/min converge more rapidly, resulting in almost the same temperature 10 mm away from the center. For  $V_p$  of 1 m/min this effect is less pronounced, resulting in elevated temperatures of  $\approx 200^\circ\text{C}$  at equal distances same distance. This effect might be attributed to several different causes with one of them being the thermal conductivity of Mg. Kainer et al. sets the thermal conductivity of Mg to  $156 \text{ W / (m K)}$

which is comparably slow.<sup>[28]</sup> As the tool represents the only heat source, the slow conductivity results in almost no heating of the material in front of the tool and limited heat flux to the sides. The limited heat flux to the front of the tool yields that during processing, cold material is fed into the process zone resulting in further cooling. The effects of limited heat flux to the sides is particularly interesting when regarding the recrystallization behavior. As stated by Fatemi-Varzaneh et al. and Braszczyńska-Malik et al. Mg recrystallizes at temperatures starting at  $\approx 200^{\circ}\text{C}$ .<sup>[29,30]</sup> Using this information it is possible to calculate isotherms of the heat flux around the tool for different  $V_p$ . This gives a size approximation of the area in which recrystallization for the mechanically deformed zones as well as annealing for the thermally affected zones may take place. Isotherms for different  $V_p$  can be seen in Fig.10. Fig.10 a) depicts the  $200^{\circ}\text{C}$  isotherms for  $V_p$  of 1, 5 and 10 m/min. It can be seen, that for  $V_p$  of 1 m/min, the isotherms outreach the radius ( $r$ ) of the shoulder in front of the tool and orthogonal to PD. This changes when increasing  $V_p$  to 5 m/min and above as the isotherms no longer exceeds the shoulder radius in any direction. Fig.10 b) shows the  $320^{\circ}\text{C}$  isotherms, encircling the area in which annealing can take place.

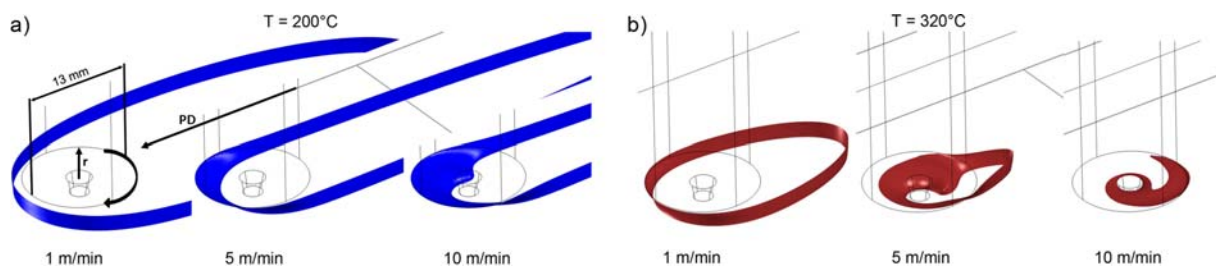


Figure 10: Comparison of isotherms at  $200^{\circ}\text{C}$  a) and  $320^{\circ}\text{C}$  b) for different processing speeds (1 - 10 m/min).

For Vp of 1 m/min, the isotherms do not exceed the shoulder radius in front of the tool. Perpendicular to the processing direction, the isotherm spread well over the tool radius and taper towards the end. The thermal field for samples processed at Vp of 5 m/min, looks similar to the one of 1 m/min with the difference that the temperature field never exceeds the tool radius and the thermal tail shortens. For samples processed at 10 m/min, cold material is introduced into the weld zone more rapidly resulting in a size reduction of the heated region. The closed isotherm which was still clearly observable in the 5 m/min samples is reduced to a small location directly around the pin. The trailing temperature tail is no longer visible as only a small region under the shoulder on the AS reaches 320°C.

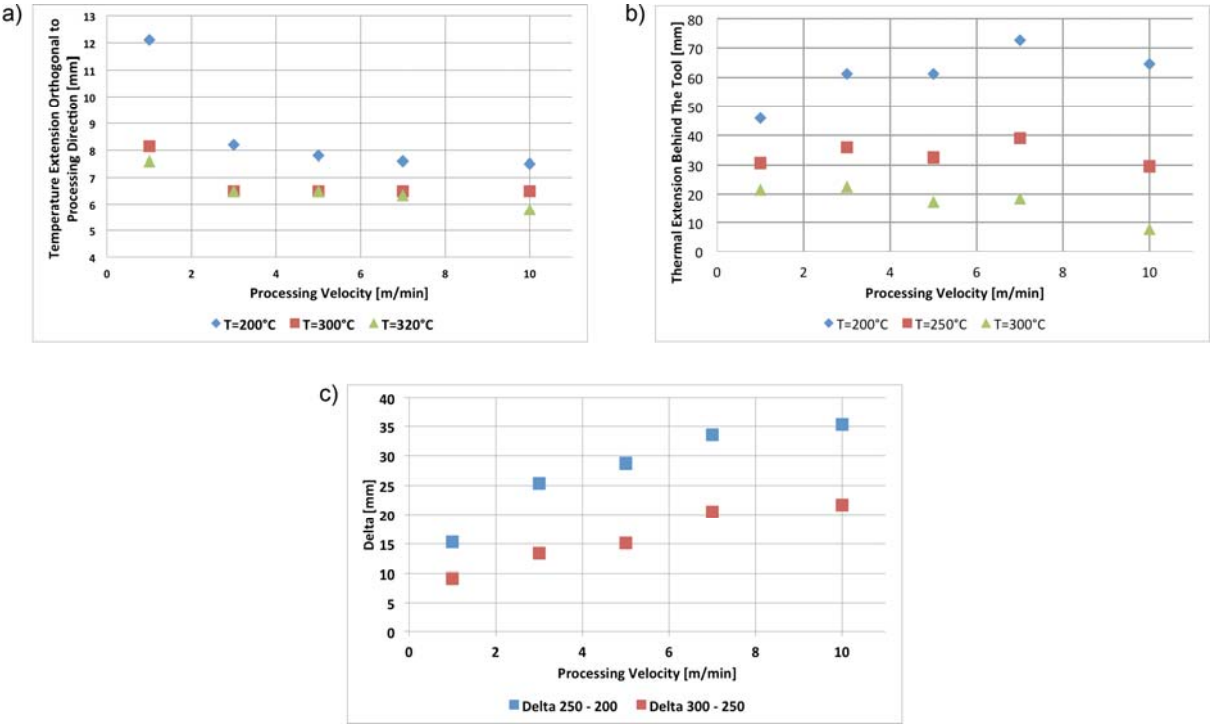


Figure 11: Comparison of the maximum extension of 200° C, 300° C and 320° C isotherms orthogonal to processing direction. The distance is measured from the weld center to the isotherm a). Comparison of the trailing temperature tail length behind the tool b). The difference ( $\Delta$ ) between 200° C and 250° C as well as 250° C and 300° C c).

Fig.11 a) shows a detailed picture of the maximum isotherm temperature extension orthogonal to processing direction in correlation to  $V_p$ . The greatest reduction in the extension can be seen in the transition between 1 and 3 m/min. For the metallurgically interesting temperatures around 320°C only small changes in thermal extension for  $V_p$  above 1 m/min are to be noted. The overall decrease, reaching a threshold at  $V_p$  of 5 m/min, can be correlated to the decrease in EIUL. Fig.11 b) depicts the distance of the trailing temperature tail. Compared to the thermal extension orthogonal (Fig.11 a)) to the length behind the tool, the 200°C isotherms for  $V_p$  of 1 m/min experience an increase.

For the 250°C isotherms in Fig.11 b) such an increase cannot be seen as the isotherms appear to have a constant length behind the tool with rising  $V_p$ . This consistency shows, that the extension of 250°C isotherm behind the tool is independent of processing parameters in the investigated regime.

The 300°C isotherms on the other hand appear to be decreasing with increasing  $V_p$ . This might be correlated to the declining RPM/ $V_p$  ratio reducing the overall heat input. Phenomenologically this effect can be described as a shortening of the extension due to the dominance of the feeding of cold material into the event horizon of the tool.

When interpreting these results, the following aspects must be taken into account: The results shown in Fig.11 b) are numerical in nature, thus it must be noted that the length of a potential scatter band is unknown. In order to put the results shown in Fig.11 b) into perspective, a difference between 200°C and 250°C as well as 250°C and 300°C was calculated. This difference ( $\Delta$ ) was then plotted over processing speed as seen in Fig.11 c). A steady increase for both  $\Delta$  reaching a threshold at  $V_p$  of 7 m/min can be seen. This could give insight into a potential scatter band giving

rise to the argument that the results for  $V_p$  of 7 m/min and 10 m/min in Fig.11 b) differ only in magnitude but not in relation to each other.

Summarizing it can be noted that the length of the trailing temperature tail is an important factor for tailoring the microstructure as it defines how long recrystallization and annealing processes may take place in the respective zones. The longer the tail becomes in a respective temperature regime, the longer the material can recrystallize, anneal or recover in the respective areas. This results in the formation and growth of grains in the SZ and partly in the TMAZ as well as potential grain growth or recovery in the HAZ. As both processes depend on the amount of thermal energy as well as the time that this energy is available, the ability to control it is crucial.

#### 4.4. Microstructure and Texture Analysis

The effect of processing parameters (mechanical strain, thermal input) on the grain size and shape as well as texture evolution has been determined using EBSD analysis. Herein the SZ in the center of the process zone has been investigated by cutting the samples orthogonal to processing direction (PD).

##### Microstructural evolution

During FSP the microstructure experiences several deformation stages in which recovery and recrystallization processes can take place depending on plastic strain and temperature gradients imposed on the material. In this study the resulting microstructure and texture in the SZ are strongly influenced by the chosen process

parameters as seen in Fig.12. The grain boundaries are divided into low angle boundaries (LAB) and high angle boundaries (HAB). LAB have a range of 2° - 15° and the HAB of 15° - 180°. The average base material grain size is  $\approx 6 \mu\text{m}$  as listed in Tab.2. The base material microstructure appears fully recrystallized as almost no twins and only a small amount of LAB are visible.

Table 2: Grain size and LAGB values of the base material and SZ of processed samples.

/	BM	1 m/min	5 m/min	10 m/min
Grain Size [ $\mu\text{m}$ ]	5.9	3.8	2.3	2.4
LAB [%]	16.8	17.8	21.8	38.4

At  $V_p$  of 1 m/min (Fig.12 b)) the average grain size decreases to  $\approx 4 \mu\text{m}$  accompanied by a slight increase in the LAB fraction. Evidence of discontinuous recrystallization can be seen as some fine grains are emerging at LAB within larger grains as well as on HAB as indicated by the arrow.

For  $V_p$  of 5 m/min (Fig.12 c)) the grain size is further reduced to  $\approx 2 \mu\text{m}$ . As previously seen in Fig.12 b), the grains are clearly distinguishable from each other with an increased amount of small recrystallized grains. The LAB fraction is further increased reaching 21.8%. Reaching  $V_p$  of 10 m/min (Fig.12 d)) the grain morphology changes giving rise to a more serrated form factor. Compared to samples processed with 5 m/min (Fig.12 c)) the grain sized does not change leading to the conclusion that a threshold is being reached. This threshold might arise from the comparable RPM/ $V_p$  ratio exhibited by the two samples. On the other hand, the LAB fraction continuously rises to over 38%. Interestingly no twins were found in the SZ of any of the processed samples.

This grain size / LAB divergence might be due to the different recrystallization dynamics of the samples as discussed below. As previously investigated by Suhuddin et al. using stop action experiments the discontinuous recrystallization of the material mainly takes place in the region directly in front of the pin.<sup>[31]</sup> In a second step, these discontinuously recrystallized grains are moved around the tool by the pin and deposited behind the tool.

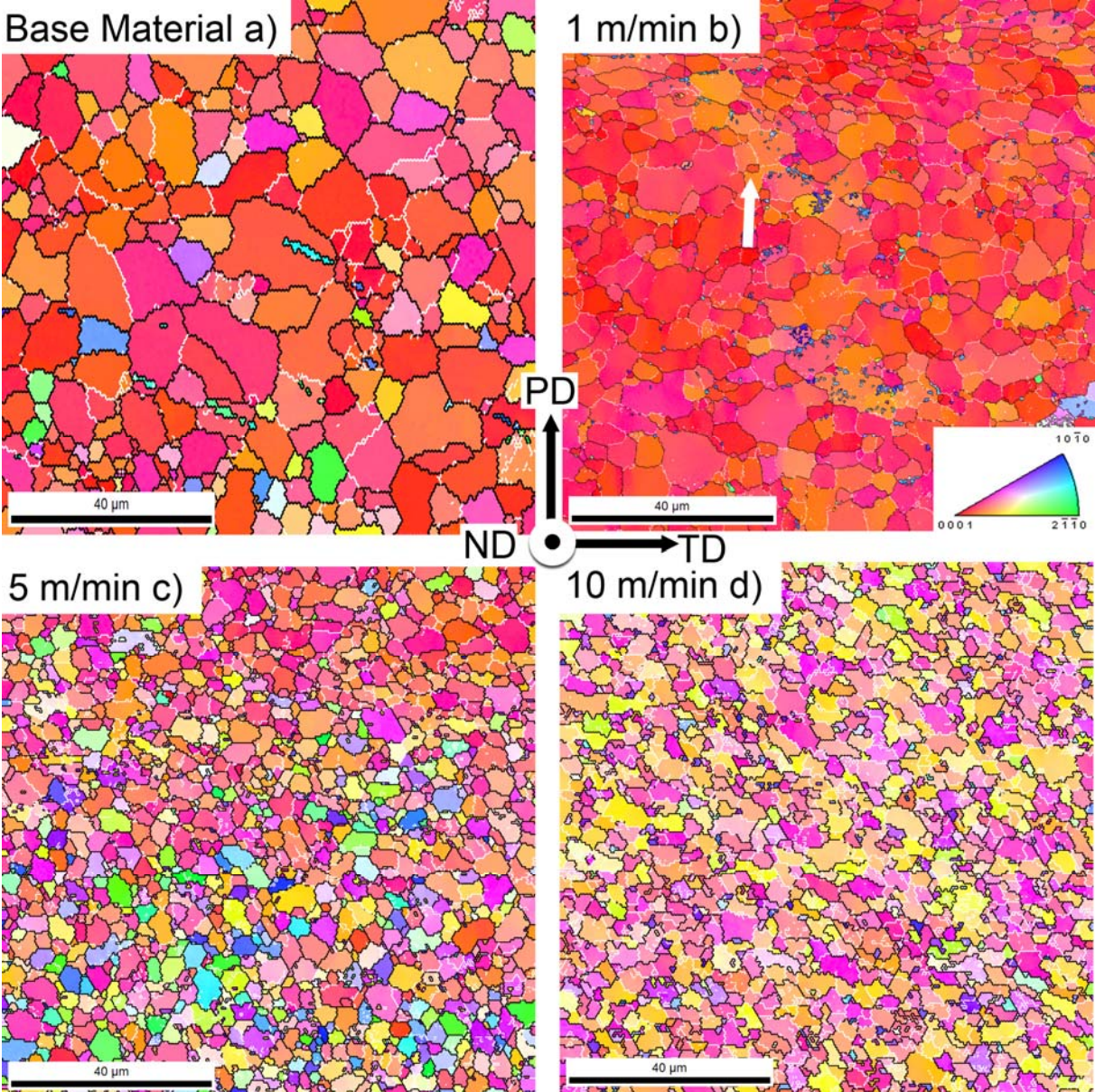


Figure 12: EBSD maps illustrating the base material a) as well as the SZ of samples processed at 1 b), 5 c) and 10 d) m/min. LAB are depicted in white, HAB are depicted in black.

During this movement, the grains can be broken up and or plastically strained. Once the grains are deposited behind the pin, the amount of recovery and potential grain growth of these grains is solely dependent on the residual temperature and the introduced amount of plastic strain. As seen in section 4.3, the maximum temperature as well as the length of the maximum extension continuously decreases with increasing  $V_p$ . Additionally one can argue, that the amount of low temperature deformation is increasing with decreasing RPM/ $V_p$  ratio. As a result, the discontinuous recrystallization in terms of LAB development for  $V_p$  of 1 m/min (Fig.12 b)) is lacking sufficient thermal energy for grain growth, yielding a reduction in grain size.

Similarly, the grain size reduction for  $V_p$  of 5 m/min (Fig.12 c)) can be attributed to discontinuous recrystallization in front of the tool, but yielding further limited grain growth after the tool has passed due to the lower temperatures in the process zone. The lower process temperatures accompanied by a decreased RPM/ $V_p$  ratio yields an increase in LAB. The grain size reduction reaches a threshold between  $V_p$  of 5 and 10 m/min at  $\approx 2 \mu\text{m}$  as the amount of thermal energy (Fig.9 a)) reaches comparable values and does not suffice for grain growth. As described above, differences in the grain morphology are visible in the samples processed with  $V_p$  of 10 m/min (Fig.12 d)) resembling a serrated grain structure in which grains previously separated by a HAB are now replaced by LABs. This change in morphology yields the hypothesis that the grain which undergo discontinuous recrystallization in front of the tool, are heavily plastically deformed as they are moved around the tool and deposited behind the tool. As for the 10 m/min samples the RPM/ $V_p$  ratio, and with it the amount of thermal energy is further reduced, the serrated grain structure remains.

## Texture evolution

During FSP, the texture of the SZ continuously changes. The base material experiences a typical  $\{0002\}$  basal texture as expected for sheet material after a rolling process as seen in Fig.13 a). This is confirmed by the circular intensity distribution of the  $\{10\bar{1}0\}$  family as shown by the inverse pole figures in Fig.14 a).

Compared to the base material texture the SZ texture of samples processed at  $V_p$  of 1 m/min (Fig.13 b)) exhibits a slight change. Even though the basal texture of the base material remains, it is intensified and randomization is reduced (Fig.14 b)). Scattered intensities are visible in the  $\langle 10\bar{1}0 \rangle$  direction with the (0001) pole remaining predominant.

At  $V_p$  of 5 m/min the (0001) intensity pole is still dominant but exhibits a shifts out of plane into the PD direction (Fig.13 c)). The ring structure seen in the base material on the  $(10\bar{1}0)$  plane changes in this course to a band like intensity distribution indicating a rotational symmetry. Fig.14 c) depicts this movement as the intensity distribution moves away from the  $\langle 0001 \rangle$  to the  $\langle 10\bar{1}0 \rangle$  and  $\langle 2\bar{1}\bar{1}0 \rangle$  direction.

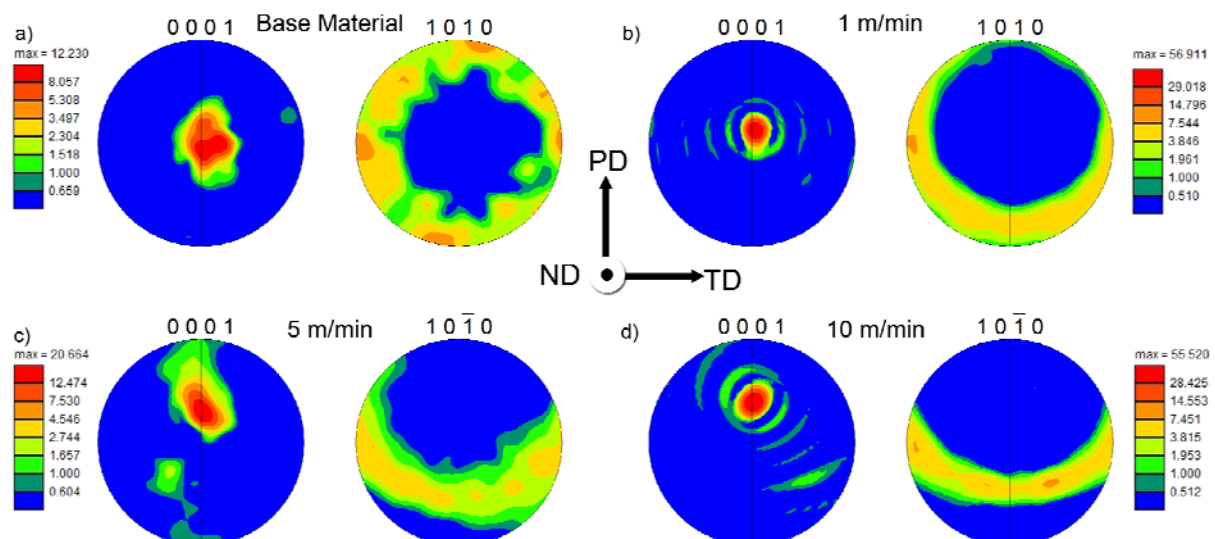


Figure 13: (0001) and  $(10\bar{1}0)$  pole figures of: Base material a) and the SZ of samples processed at 1 b), 5 c) and 10 m/min d)

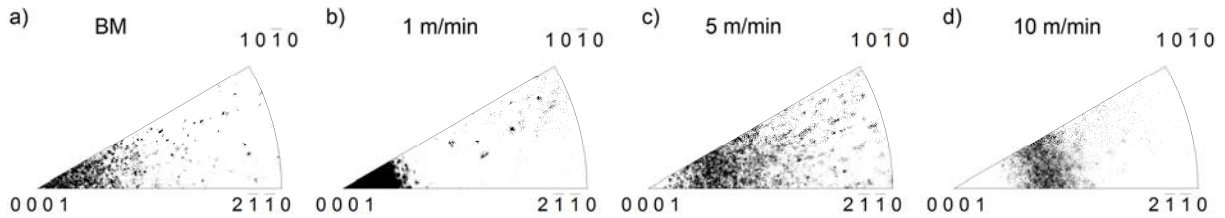


Figure 14: Inverse pole figures of the of: Base material a) and the SZ of samples processed at 1 b), 5 c) and 10 m/min d).

As the  $V_p$  increases to 10 m/min, the above described effect becomes more pronounced. In addition to the robust intensity maximum movement towards PD (Fig.13 d)) the increased randomization seen in Fig.14 c) is significantly reduced in Fig.14 d).

This indicates that an increase in plastic strain, initiated by the reduction in the RPM/ $V_p$  ratio, has a sizeable effect on the texture evolution yielding a shift of the basal plane towards the PD direction. This shift is accompanied by the evolution of a  $\{10\bar{1}0\}$  band like structure. As deformation is preferably done by basal slip, the above results imply that a knowledge based modification of the microstructure and texture might lead to an improvement in formability.

## 5. Summary

1. High Speed Friction Stir Processing was successfully performed on Mg AZ31 in a range between 1 and 10 m/min.
2. Using a TPM heat source model, the energy input per unit length (EIUL) was calculated. Good weld qualities could be obtained at a continuous decrease in (EIUL) while increased processing speed.
3. Image correlation on the deformed samples revealed a continuous decrease of the samples maximum distortion at increasing processing speeds.
4. Thermal analysis revealed a strong asymmetry between the AS and RS which grew stronger with increasing processing speed. Depending on processing speed the temperatures directly under the tool ranged between 470°C and 300°C thus being in the range of the hot working temperature. At increasing processing speeds the length of the isothermal tail behind the tool showed a diverging devolution for the investigated temperatures.
5. EBSD observations revealed a continuously decreasing grain size with increasing processing speed.

Between 5 m/min and 10 m/min the grain size reached a threshold. The samples grain morphology in the SZ appears equiaxed with the exception of the 10 m/min sample which shows a serrated grain shape. The basal texture of the base material gradually shifts with increasing processing speed into the processing direction reaching a maximum at a tilt angle of 45°. LABs increased with increasing processing speed indicating a limit of the dynamic recrystallization.

- [1] D. Eliezer, E. Aghion, F. S. Froes, *Adv. Perform. Mat.* **1998**, 5, 201-212.
- [2] E. Aghion, B. Bronfin, D. Eliezer, *Journ. Mater. Process. Tech.* **2001**, 117, 381-385.
- [3] L. Bichler, C. Ravindran, *Mat. Char.* **2010**, 61, 296-304.
- [4] D. Fechner, N. Hort, K.U. Kainer, in *MAGNESIUM TECHNOLOGY 2009*, **2009** pp. 111-116.
- [5] H. Friedrich, S. Schumann, *Journ. Mater. Process. Tech.* **2001**, 117, 276-281.
- [6] M. Kulekci, *Int. Journ. Adv. Manuf. Tech.* **2008**, 39, 851-865.
- [7] S. Kleiner, E. Ogris, O. Beffort, P.J. Uggowitzer, *Adv. Eng. Mat.* **2003**, 5, 653-658.
- [8] M. Barnett, *Mat. Sci. Eng. A* **2007**, 464, 1-7.
- [9] M. Barnett, *Mat. Sci. Eng. A* **2007**, 464, 8-16.
- [10] K. Matsubara, Y. Miyahara, Z. Horita, T. G. Langdon *Act. Mat.* **2003**, 51, 3073-3084.
- [11] H. Watanabe, T. Mukai, K. Ishikawa, K. Higashi, *Script. Mat.* **2002**, 46, 851-856.
- [12] I. Charit, R. Mishra, *Mat. Sci. Eng. A* **2003**, 359, 290-296.
- [13] R. Mishra, M. Mahoney, in *Friction Stir Welding and Processing*, ASM International, **2007**.
- [14] W. Thomas, E. Nicholas, J. Needham, M. Murch, P. Templesmith, C. Dawe, in *Improvements to friction welding*, GB-Patent, **1992**.
- [15] R. Mishra, M. Mahoney, S. McFadden, N. Mara, A. Mukherjee, *Script. Mat.* **1999**, 42, 163-168.
- [16] J. Esparza, W. Davis, L. Murr, *Journ. Mat. Sci.* **2003**, 38, 941-952.
- [17] C. Chang, X. Du, J. Huang, *Script. Mat.* **2008**, 59, 356-359.
- [18] R. Gehrman, M. Frommert, G. Gottstein, *Mat. Sci. Eng. A* **2005**, 395, 338-349.
- [19] T. Mukai, M. Yamanoi, H. Watanabe, K. Higashi, *Script. Mat.* **2001**, 45, 89-94.
- [20] X. Cao, M. Jahazi, *Mat. Des.* **2009** 30, 2033-2042.
- [21] X. Cao, M. Jahazi, J. Immarigeon, W. Wallace, *Journ. Mater. Process. Tech.* **2006** 171, 188-204.
- [22] GOM-GmbH Pontos 3D Analysis - <http://www.gom.com/metrology-systems/3d-motion-analysis.html> **2012**.
- [23] TSL OIM Analysis 5.31 Help, **2008**.
- [24] J. Hilgert, H. Schmidt, J. dosSantos, N. Huber, *Journ. Mater. Process. Tech.* **2011**, 211, 197-204.
- [25] H. Schmidt J. Hattel, *Comsol Conference 2008* **2008**.
- [26] M. Avedesian, H. Baker, in *Magnesium and Magnesium Alloys*, ASM Specialty Handbook, **1999**, 258-259.
- [27] H. Friedrich, B. Mordike in *Magnesium Technology*, Springer, **2006**.
- [28] K. Kainer, in *Magnesium alloys and Technology*, Wiley-VCH, **2003**, 2.
- [29] S. Fatemi-Varzaneh, A. Zarei-Hanzaki, H. Beladi, *Mat. Sci. Eng. A* **2007**, 456, 52-57.
- [30] K. Braszczyńska-Malik, *Journ. Allo. Comp.* **2009**, 477, 870-876.
- [31] U. Suhuddin, S. Mironov, Y. Sato, H. Kokawa, C. Lee, *Acta Mat.* **2009**, 57, 5406-5418.